Membrane Horizons
https://www.sciltp.com/journals/mh

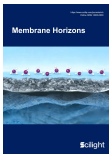

Article

Optimization of Reverse Osmosis Concentration for High-Salinity Iron Phosphate Wastewater

Xifeng Yan [1,2], Suhang Kong [1], Mi Deng [3], Haofei Chen [1] and Yong Wang [4,*]

[1] School of Water Resources and Environmental Engineering, East China University of Technology, Nanchang 330013, China
[2] National Key Laboratory of Uranium Resources Exploration-Mining and Nuclear Remote Sensing, Nanchang 330013, China
[3] Institute of Microbiology, Jiangxi Academy of Sciences, Nanchang 330096, China
[4] Hangzhou Tianchuang Environmental Technology Co., Ltd., Hangzhou 311121, China
* Correspondence: wangyo@hztchj.com

How To Cite: Yan, X.; Kong, S.; Deng, M.; et al. Optimization of Reverse Osmosis Concentration for High-Salinity Iron Phosphate Wastewater. *Membrane Horizons* **2026**, *1*(1), 3.

Received: 13 March 2026
Revised: 30 April 2026
Accepted: 2 June 2026
Published: 23 June 2026

Abstract: This study investigates reverse osmosis (RO) concentration for high-salinity iron phosphate wastewater, with emphasis on osmotic pressure behavior, water permeability, concentration enhancement, and fouling control. The measured osmotic pressure increased markedly with total dissolved solids (TDS) and deviated by 18–25% from the ideal van't Hoff prediction at high ionic strength. A temperature-corrected osmotic-pressure model ($R^2 = 0.987$) and a ternary quadratic permeability-coefficient model ($R^2 = 0.99$) were established. The water permeability coefficient ranged from 3.7 to 12.0 $L \cdot MPa^{-1} \cdot m^{-2} \cdot h^{-1}$. To extend the RO concentration limit, an RO5+RO7 staged configuration was proposed. In this study, the term "micro-osmosis membrane process" is used specifically for a two-stage RO configuration in which a high-rejection RO5 element is followed by a lower-rejection RO7 element. Unlike conventional staged RO using the same high-rejection membrane in both stages, the RO7 element deliberately permits limited salt passage to the permeate side, thereby lowering the effective osmotic-pressure difference across the second-stage membrane without adding an external draw solution. Compared with the conventional RO5+RO5 configuration, this design increased the concentration endpoint by 8.4%. Membrane autopsy by SEM-EDS indicated that the dominant fouling was Fe-Mn-Ca composite scaling. A targeted two-step cleaning strategy, consisting of 1% tetrasodium EDTA + 0.5% ammonia water + 0.1% sodium hexametaphosphate alkaline cleaning followed by 2% citric acid acid washing, restored the flux recovery rate to >94% and salt rejection to 99.7%. These results provide a practical RO concentration and cleaning strategy for high-salinity iron phosphate wastewater treatment.

Keywords: reverse osmosis; iron phosphate wastewater; osmotic pressure; membrane fouling; cleaning process

1. Introduction

With the rapid development of the new energy industry, iron phosphate, as a precursor for cathode materials of lithium-ion batteries, has been produced on an increasingly large scale [1–8]. Consequently, the treatment of high-salinity and high-concentration iron phosphate wastewater generated during production has become an increasingly prominent issue [9–12]. Such wastewater is characterized by high total dissolved solids (TDS), and the coexistence of metal ions (Fe, Mn, Ca, etc.) with phosphate and sulfate ions. Direct discharge not only wastes water resources but also causes serious harm to the ecological environment. Therefore, achieving resource

utilization and zero discharge of iron phosphate wastewater has become critical to the sustainable development of the industry, and how to treat such wastewater economically and efficiently has become a common concern in both academia and industry.

Reverse osmosis (RO) membrane separation technology has been widely used in industrial wastewater treatment due to its high salt rejection rate and simple operation [13]. However, for high-concentration iron phosphate wastewater, the traditional single-stage reverse osmosis process suffers from engineering problems such as low concentration limit, serious membrane fouling, and high operating energy consumption. Most existing studies focus on the treatment of low-concentration wastewater and lack systematic mechanism modeling and efficient cleaning strategies for the reverse osmosis process of high-concentration iron phosphate wastewater. Research on osmotic pressure characteristics, membrane fouling mechanism, and process optimization at high concentrations is still insufficient [14–19], which makes it difficult to support the efficient implementation of zero-discharge projects for such wastewater and restricts the green development of the iron phosphate industry. Therefore, it is urgent to carry out research on the mechanism and process optimization of reverse osmosis for high-concentration iron phosphate wastewater.

Despite extensive research on RO treatment of saline industrial effluents, several issues remain unresolved for high-strength iron phosphate wastewater from the lithium battery supply chain. Existing studies mainly address general high-salinity brines or relatively low-strength iron phosphate wastewater, whereas the simultaneous effects of ultra-high osmotic pressure, Fe-Mn-Ca-phosphate/sulfate scaling, and multi-stage RO configuration have rarely been examined using real industrial effluents. In engineering applications, these coupled factors cause rapid flux decline, frequent chemical cleaning, and limited recovery. In addition, osmotic-pressure prediction for such multi-component electrolytes has seldom been validated experimentally, which limits accurate pressure design and stable operation. Therefore, a process-oriented study integrating osmotic-pressure modeling, permeability prediction, membrane configuration optimization, and fouling control is required.

Recent studies from 2022–2025 have advanced high-salinity wastewater treatment [20–22], permeability prediction, membrane-process simulation [23,24], chemical cleaning [25–27], and resource utilization [28,29], as well as RO transport theory, membrane fouling control, electrolyte non-ideality, and confined-water dynamics in polyamide membranes [30–34]. These studies provide useful guidance for multi-stage RO design, pressure-driven water transport, membrane autopsy, and chemical cleaning. Nevertheless, their findings have not been systematically adapted to high-concentration iron phosphate wastewater, in which ammonium, sulfate, phosphate, Fe, Mn, and Ca coexist and generate strong non-ideal electrolyte behavior and composite scaling. This study addresses this application-specific gap.

In this study, the pretreated effluent from iron phosphate production filtrate supplied by Hubei Xingyou New Energy Technology Co., Ltd. (Hubei Province, China) was used as the research object. The novelty of this work lies in coupling measured osmotic-pressure behavior of real iron phosphate wastewater with a deliberately asymmetric RO5+RO7 staged configuration and a fouling-specific cleaning strategy, rather than simply applying conventional staged high-pressure RO.

The specific objectives of this study are:

- To establish and validate osmotic-pressure and water-permeability prediction models for high-concentration iron phosphate wastewater.
- To evaluate an RO5+RO7 micro-osmosis membrane configuration for increasing the RO concentration endpoint.
- To identify the dominant Fe-Mn-Ca composite fouling mechanism and develop a targeted chemical cleaning strategy.

By systematically investigating the variation law of wastewater osmotic pressure with concentration and temperature, optimizing the parameters of the membrane combined process, and screening and verifying high-efficiency cleaning formulas, this study aims to provide a theoretical basis and technical support for the engineering application of reverse osmosis concentration of high-salinity iron phosphate wastewater, which is of great significance for promoting the resource treatment of high-salinity wastewater in the new energy industry.

2. Materials and Methods

2.1. Materials

The experimental water was real pretreated effluent from the iron phosphate production filtrate supplied by Hubei Xingyou New Energy Technology Co., Ltd. (Wuhan, China), rather than synthetic wastewater. The main components included sulfate, ammonia nitrogen, and dihydrogen phosphate (expressed as total phosphorus), and the detailed water-quality analysis is presented in Table 1.

Chemicals: Sodium hydroxide (NaOH), ammonia water, 4Na-EDTA, sodium hexametaphosphate, sodium tripolyphosphate, oxalic acid, sodium bisulfite, and sodium dodecyl sulfate (SDS) were used in this study. All reagents were of analytical grade and used as received without further purification.

Instruments: A Hangzhou Tianchuang membrane performance tester was employed for osmotic-pressure and membrane-performance evaluation. The permeability-coefficient tests were performed using membrane sheets dissected from DuPont FilmTec SW30XFR-400/34i seawater extra fouling-resistant RO elements. According to the DuPont product data sheet [35], SW30XFR-400/34i has an active area of 400 ft^2 (37 m^2), a 34 mil feed spacer, a permeate flow rate of 7500 GPD (28.4 $m^3 \cdot d^{-1}$), a stabilized NaCl rejection of 99.8%, a minimum NaCl rejection of 99.65%, and a stabilized boron rejection of 92% under standard seawater test conditions. The engineering-scale verification system used DuPont FilmTec SW30HRLE-400 seawater RO elements, and the design membrane area used for system-scale calculation was 37 m^2 per element according to the engineering design data. Therefore, the value of 37 m^2 per element refers to the DuPont seawater RO membrane-sheet and engineering-verification calculation, rather than to the Veolia RO5 or RO7 elements used in the staged concentration test. A TC-8040 high-pressure membrane separation system equipped with commercial 8040 spiral-wound RO elements was used for the staged concentration experiments. The RO5 and RO7 elements were Industrial RO membranes supplied by Veolia Water Technologies & Solutions (formerly GE/SUEZ). According to the Veolia product information [36], Industrial RO5 8040F50 has an average flow rate of 7400 GPD (28.0 $m^3 \cdot d^{-1}$), an average NaCl rejection of 99.5%, an effective membrane area of 269 ft^2 (25.0 m^2), a 50 mil (1.27 mm) feed spacer, a maximum operating pressure of 1200 psi (80 bar), and a maximum operating temperature of 50 °C. Industrial RO7 8040F35 has an average flow rate of 10,500 GPD (39.7 $m^3 \cdot d^{-1}$), an average NaCl rejection of 92%, an effective membrane area of 330 ft^2 (30.7 m^2), a 35 mil (0.89 mm) feed spacer, a maximum operating pressure of 1200 psi (80 bar), and a maximum operating temperature of 50 °C. The commercial RO elements used in this study were polyamide thin-film composite membranes; their separation layer was an aromatic polyamide active layer supported by a porous polymeric substrate. These specifications distinguish RO7 as a lower-rejection RO element rather than an NF element. SEM-EDS was used to characterize membrane fouling and elemental composition. An atomic absorption spectrophotometer and an ultraviolet spectrophotometer were applied to determine metal ions and other water-quality parameters, respectively.

Table 1. Raw water quality of iron phosphate wastewater.

No.	Test Item	Filtrate
1	pH	1.77
2	Sulfate	53.6 $g \cdot L^{-1}$
3	Ammonia nitrogen	13.5 $g \cdot L^{-1}$
4	Total phosphorus	1376 $mg \cdot L^{-1}$

2.2. Methods

Osmotic Pressure Measurement: The membrane osmotic method was adopted because it directly measures equilibrium pressure and is more suitable than ideal TDS-based calculation for concentrated multi-component electrolyte wastewater. The raw water used in this study was real industrial wastewater; only the concentration-gradient osmotic-pressure test was prepared by evaporating the pretreated filtrate to obtain dissolved solids and then reconstituting the solids to 5–200 $g \cdot L^{-1}$. This approach maintained the main inorganic salt matrix of the original filtrate while allowing controlled concentration gradients. Possible changes in volatile components during drying were considered as a limitation when interpreting the osmotic-pressure model. The pressure at osmotic equilibrium was recorded using a Hangzhou Tianchuang membrane tester (Figure 1), with temperature controlled at ±0.5 °C.

Membrane Performance Test: The water-permeability coefficient model was developed from membrane-performance tests using membrane sheets dissected from DuPont FilmTec SW30XFR-400/34i seawater RO elements, whose full-element product data list an active area of 400 ft^2 (37 m^2) and a 34 mil feed spacer. The 8040 high-pressure membrane separation unit is shown in Figure 2, and the membrane concentration/permeate circulation mode is shown in Figure 3. The effects of temperature T (15, 25, and 35 °C), membrane surface flux F (8, 12, and 16 LMH), and feed concentration C (50, 100, and 150 $g \cdot L^{-1}$) on water permeability coefficient A ($L \cdot MPa^{-1} \cdot m^{-2} \cdot h^{-1}$) and salt rejection R (%) were investigated. For each operating condition, the membrane system was operated until feed pressure, permeate flow, and permeate conductivity reached stable values. Independent triplicate experiments were not conducted because the experiments used real industrial wastewater and large-volume membrane-performance testing; therefore, the reported values are stabilized operating data rather than

mean ± SD results. The relationship was fitted using a ternary quadratic equation and the least-squares method, as shown in Equation (1). An L27(3^3) orthogonal design was used, and nonlinear regression was conducted in Python 3.10 using the open-source NumPy and SciPy libraries (NumPy 1.24.3 and SciPy 1.10.1, scipy.optimize.curve_fit). The fitted model was further verified using actual operating data from an engineering-scale membrane system treating the same type of iron phosphate wastewater.

$$A = a1T^2 + a2C^2 + a3F^2 + a4TC + a5CF + a6TF + a7T + a8C + a9F + a10 \quad (1)$$

A: Water permeability coefficient, unit: $L \cdot MPa^{-1} \cdot m^{-2} \cdot h^{-1}$;
T: Operating temperature, unit: °C;
C: Total dissolved solids, unit: $g \cdot L^{-1}$;
F: Membrane surface flux, unit: $L \cdot m^{-2} \cdot h^{-1}$;
a1–a10: Model coefficients obtained by regression fitting.

Figure 1. Membrane performance tester.

Figure 2. 8040 high-pressure membrane separation unit.

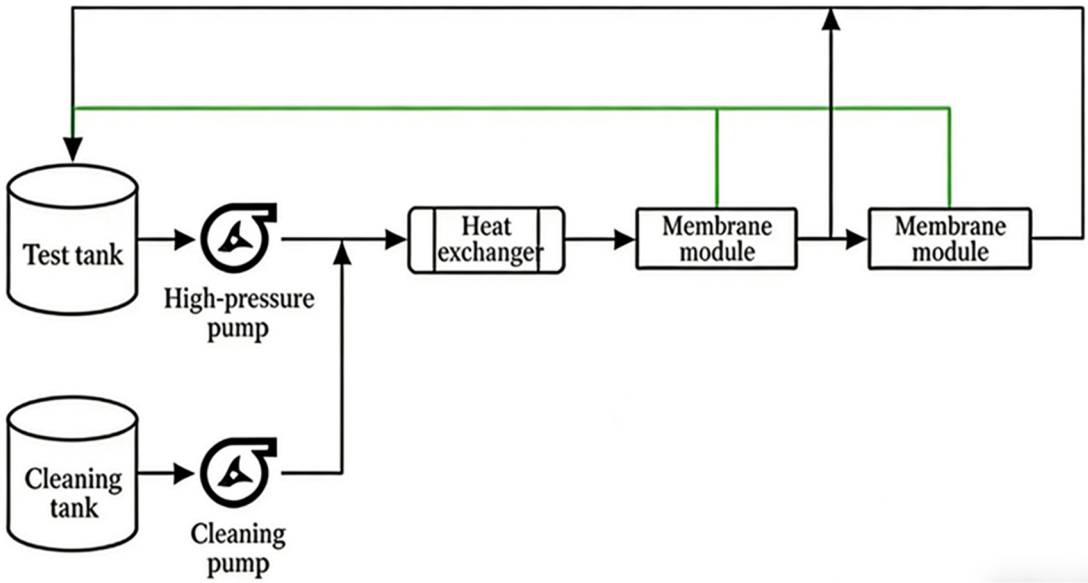

Figure 3. 8040 high-pressure membrane separation system test process.

Micro-osmosis Membrane Combined Application Test: The 8040 membrane test equipment was used with RO5 and RO7 elements. RO5 was a high-rejection industrial RO membrane, whereas RO7 was a lower-rejection industrial RO membrane with higher salt passage. In this work, "micro-osmosis" does not refer to a standard membrane category; it denotes the deliberate use of a lower-rejection RO7 element after a high-rejection RO5 element to create internal osmotic assistance. The process differs from conventional staged RO because the second stage does not use the same high-rejection RO membrane; it differs from loose RO alone because the first RO5 stage still maintains high product-water quality; and it differs from osmotically assisted RO because no external draw solution is introduced. Controlled salt passage through RO7 increases the permeate-side osmotic pressure and reduces the osmotic-pressure penalty across the second-stage membrane, thereby helping maintain positive net driving pressure at higher concentrate salinity. The process configuration and internal osmotic-relief mechanism are illustrated in Figure 4. Four feed solutions with TDS concentrations of 50, 100, 120, and 150 $g \cdot L^{-1}$ were prepared. The feed pH was adjusted to 5.5, the temperature was maintained at 25 °C, and the average endpoint permeate flux was controlled at 5 $L \cdot m^{-2} \cdot h^{-1}$. The final concentrate concentration, salt rejection, and required operating pressure were recorded.

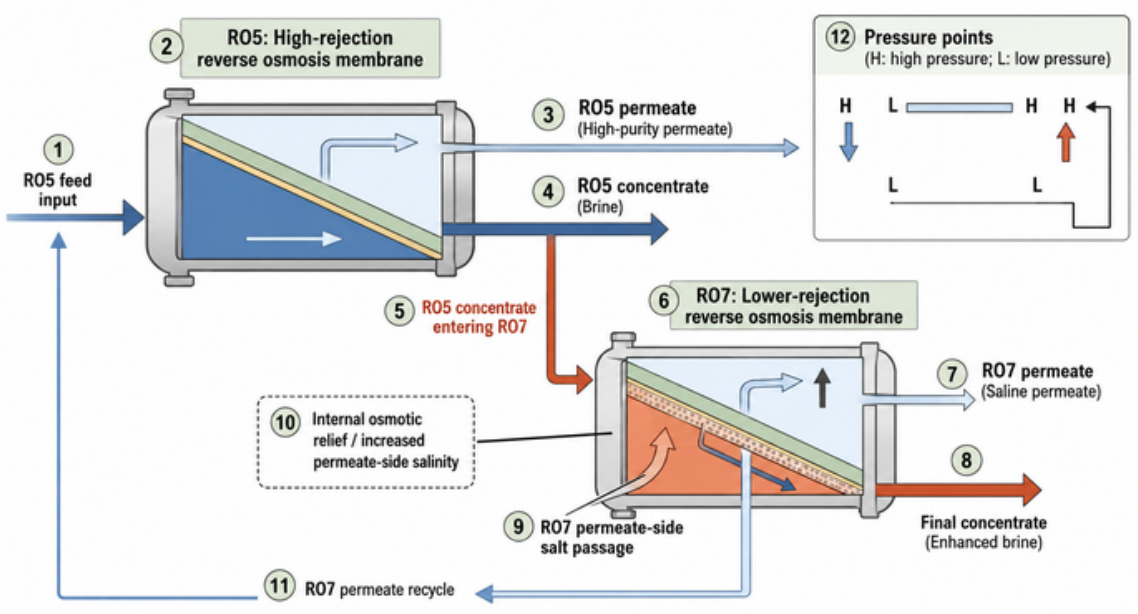

Figure 4. Schematic illustration of the RO5+RO7 micro-osmosis composite membrane process and its internal osmotic-relief mechanism.

Membrane Fouling Control Test: The fouling morphology was characterized by SEM, and its composition was analyzed by EDX. The fouled membrane element was disassembled into membrane sheets, and the pre-cleaning test was carried out using a membrane tester in accordance with the Chinese national standard GB/T 32373-2015 "Test Methods for Reverse Osmosis Membranes": the test solution was sodium chloride with a concentration of 32,000 $mg \cdot L^{-1}$, the test temperature was 25±1 °C, the test pressure was 5.5 MPa, and the pH was 8.0. Before the test, the salt rejection rate of the fouled membrane sheet was 99.33%, and the operating flux was 22.9 $L \cdot m^{-2} \cdot h^{-1}$ (the new membrane was 31 $L \cdot m^{-2} \cdot h^{-1}$). The cleaning agents were selected as follows: the chelating agent was mainly 4Na-EDTA + sodium tripolyphosphate, the surfactant was sodium dodecyl sulfate (SDS), the reducing protective agent was sodium bisulfite, the solubilizer was ammonia water, and the dispersant was sodium hexametaphosphate. Five different combinations were used, and the soaking time was selected as 2 and 4 h, respectively. The cleaning temperature was selected at 35 °C. Secondary acidic cleaning was performed using 2% citric acid, and the cleaning conditions are shown in Table 2. After cleaning, the recovery of flux and salt rejection was tested to screen the efficient cleaning agents for wastewater pollutants.

Table 2. Different cleaning conditions.

No.	Cleaning Agent Formulation	Secondary Acidic Cleaning	Cleaning Time (h)
1	0.8% 4Na-EDTA + 0.2% sodium tripolyphosphate	No	2
2	1% 4Na-EDTA + 0.5% ammonia water + 0.1% sodium hexametaphosphate	No	2
3	1% 4Na-EDTA + 0.025% SDS	No	2
4	1% 4Na-EDTA + 0.5% sodium bisulfite	No	2
5	1% 4Na-EDTA + 0.1% sodium hexametaphosphate	No	2
6	0.8% 4Na-EDTA + 0.2% sodium tripolyphosphate	Yes	2
7	1% 4Na-EDTA + 0.5% ammonia water + 0.1% sodium hexametaphosphate	Yes	2
8	1% 4Na-EDTA + 0.025% SDS	Yes	2
9	1% 4Na-EDTA + 0.5% sodium bisulfite	Yes	2
10	1% 4Na-EDTA + 0.1% sodium hexametaphosphate	Yes	2
11	0.8% 4Na-EDTA + 0.2% sodium tripolyphosphate	No	4
12	1% 4Na-EDTA + 0.5% ammonia water + 0.1% sodium hexametaphosphate	No	4
13	1% 4Na-EDTA + 0.025% SDS	No	4
14	1% 4Na-EDTA + 0.5% sodium bisulfite	No	4
15	1% 4Na-EDTA + 0.1% sodium hexametaphosphate	No	4
16	0.8% 4Na-EDTA + 0.2% sodium tripolyphosphate	Yes	4
17	1% 4Na-EDTA + 0.5% ammonia water + 0.1% sodium hexametaphosphate	Yes	4
18	1% 4Na-EDTA + 0.025% SDS	Yes	4
19	1% 4Na-EDTA + 0.5% sodium bisulfite	Yes	4
20	1% 4Na-EDTA + 0.1% sodium hexametaphosphate	Yes	4

Note: The proportions in the cleaning agent formulations are all mass ratios.

3. Results and Discussion

3.1. Osmotic Pressure Characteristics and Concentration Effects of Iron Phosphate Wastewater

Iron phosphate wastewater is a typical high-salinity industrial wastewater produced in the new energy material industry, and its osmotic pressure behavior directly determines the energy consumption and operational stability of membrane concentration systems. As shown in Figure 5, the osmotic pressure increased significantly with rising TDS concentration, while the measured values deviated noticeably from those calculated using the ideal van't Hoff equation. This deviation can be attributed to non-ideal electrolyte behavior at high ionic strength, including reduced ion activity, ion pairing, and short-range ion–ion interactions. Such behavior is commonly described using Pitzer-type activity-coefficient models, which account for interactions among ions and between

ions and solvent in concentrated electrolyte solutions [33]. Therefore, direct measurement and temperature correction are necessary for pressure design in high-salinity iron phosphate wastewater RO systems.

The effect of temperature on the osmotic pressure of iron phosphate wastewater is presented in Figure 6. Based on the experimental data, a temperature-corrected model for osmotic pressure was established:

$$\pi = \pi_{25}[1 + 0.023(T - 25)] \quad (2)$$

π: Osmotic Pressure at the Target Temperature, unit: bar
π_{25}: Osmotic Pressure at the Target Temperature of 25 °C, unit: bar
T: Target Operating Temperature, unit: °C

The coefficient of determination was $R^2 = 0.987$, indicating high fitting accuracy. For 150 $g \cdot L^{-1}$ wastewater, the osmotic pressure increased by approximately 2.1 bar when temperature increased by 10 °C. Therefore, temperature elevation does not reduce osmotic pressure; instead, its operational benefit lies in enhancing membrane water permeability and reducing solution viscosity, which can lower the hydraulic pressure required to maintain a target flux. This clarification is important for pressure design because the osmotic-pressure term and membrane-permeability term affect net driving pressure in opposite ways.

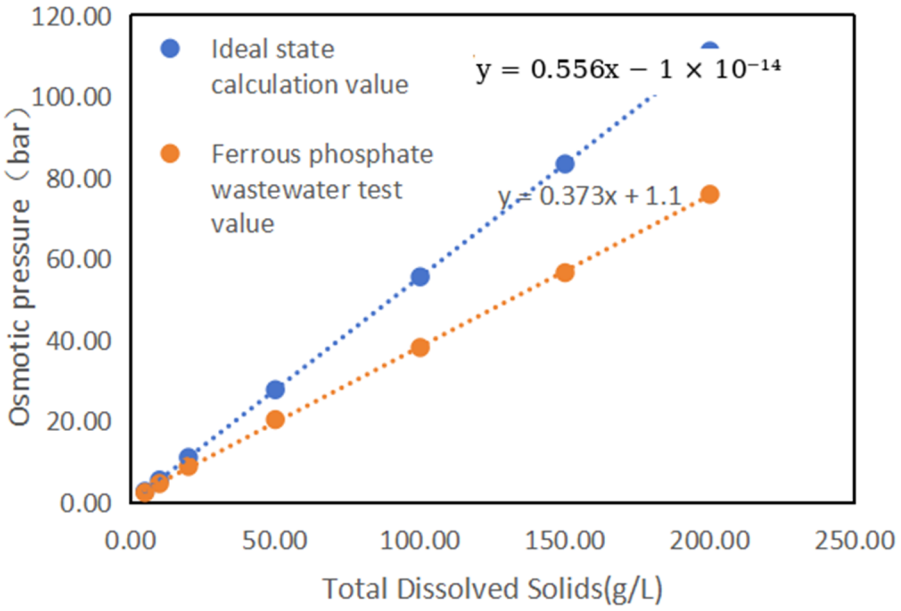

Figure 5. Comparison between Fitted Curves of Osmotic Pressure Measurements and Ideal Calculated Values for Iron Phosphate Wastewater.

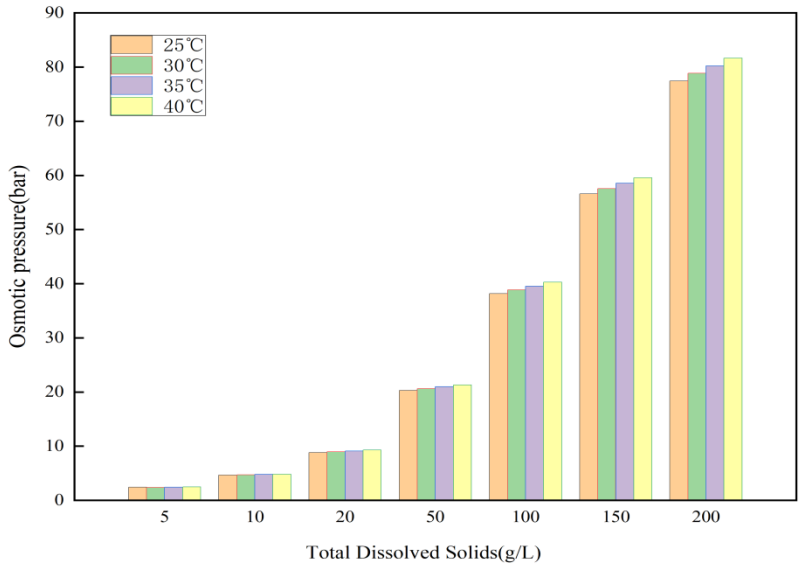

Figure 6. Effect of Temperature on Osmotic Pressure of Iron Phosphate Wastewater.

3.2. Water Permeability Coefficient Model

On the basis of clarifying osmotic pressure characteristics, the water permeability coefficient was further studied to provide key parameters for process design.

Through 27 groups of L27(3^3) orthogonal tests, the water permeability coefficient A under different operating conditions was determined, ranging from 3.7 to 12.0 $L \cdot MPa^{-1} \cdot m^{-2} \cdot h^{-1}$. Based on the ternary quadratic equation, nonlinear least-squares fitting was performed using the curve_fit function in the Python SciPy library, and the orthogonal experimental data are summarized in Table 3, and the regression coefficients were obtained (Table 4). The fitting coefficient was $R^2 = 0.985$ (rounded to 0.99), demonstrating that the empirical response-surface model can describe the combined effects of temperature, membrane surface flux, and feed concentration on water permeability within the tested range.

Table 3. Orthogonal Experiment on Membrane Concentration of Iron Phosphate Wastewater.

No.	T	F_p	C_f	P_f	Q_p	C_p	A	Salt Rejection
	°C	$L \cdot m^{-2} \cdot h^{-1}$	$mg \cdot L^{-1}$	MPa	$L \cdot h^{-1}$	$mg \cdot L^{-1}$	$L \cdot MPa^{-1} \cdot m^{-2} \cdot h^{-1}$	%
1	15	8	50,000	3.26	296	55	6.584	99.89%
2	25	12	50,000	3.44	444	62	8.602	99.88%
3	35	16	50,000	3.36	592	79	12.167	99.84%
4	15	8	100,000	5.32	296	118	5.329	99.88%
5	25	12	100,000	5.58	444	132	6.814	99.87%
6	35	16	100,000	5.65	592	169	8.738	99.83%
7	15	8	150,000	7.73	296	189	3.868	99.87%
8	25	12	150,000	8.83	444	212	3.787	99.86%
9	35	16	150,000	8.38	592	268	5.886	99.82%
10	15	12	50,000	3.59	444	38	7.767	99.92%
11	25	16	50,000	3.89	592	47	8.672	99.91%
12	35	8	50,000	2.76	296	153	11.188	99.69%
13	15	12	100,000	6.10	444	81	5.260	99.92%
14	25	16	100,000	6.24	592	101	6.608	99.90%
15	35	8	100,000	4.90	296	328	7.4	99.67%
16	15	12	150,000	8.73	444	130	3.911	99.91%
17	25	16	150,000	9.13	592	160	4.613	99.89%
18	35	8	150,000	7.24	296	518	5.06	99.65%
19	15	16	50,000	4.51	592	29	6.49	99.94%
20	25	8	50,000	3.00	296	91	8.377	99.82%
21	35	12	50,000	3.04	444	105	12.06	99.79%
22	15	16	100,000	7.14	592	62	4.817	99.94%
23	25	8	100,000	5.07	296	195	6.394	99.81%
24	35	12	100,000	5.27	444	222	8.270	99.78%
25	15	16	150,000	9.96	592	99	3.722	99.93%
26	25	8	150,000	7.45	296	309	4.474	99.79%
27	35	12	150,000	7.78	444	355	5.665	99.76%

Note: T: Temperature, F_p: Water Flux, C_f: Feed Salt Concentration, P_f: Feed Pressure. Q_p: Permeate Flow Rate, C_p: Permeate Salt Concentration, A: Permeability Coefficient.

To avoid overinterpreting the high R^2 value, model reliability was further evaluated using an independent engineering-scale operating dataset. The verification dataset was obtained from a project treating iron phosphate wastewater at 30 °C. The system used DuPont FilmTec SW30HRLE-400 seawater RO elements rather than the Veolia RO5 or RO7 elements used in the staged concentration experiment. The operating conditions included a feed flow rate of 159 $m^3 \cdot h^{-1}$, feed TDS of 92 $g \cdot L^{-1}$, system recovery of 43%, 210 membrane elements, and a design membrane area of 37 m^2 per element. This engineering dataset was used only to verify the permeability-coefficient

model derived from the DuPont FilmTec SW30XFR-400/34i membrane-sheet tests and should not be interpreted as an engineering-scale verification of the RO5+RO7 concentration-enhancement configuration. Under these conditions, the actual permeate flow was 68 $m^3 \cdot h^{-1}$ and the system salt rejection was 99.51%. The model predicted a total permeate flow of 68.72 $m^3 \cdot h^{-1}$, and the deviation in the required feed driving pressure was within 0.2 MPa, corresponding to a relative error below 5%. Considering fouling, concentration polarization, and temperature fluctuation during field operation, the prediction accuracy is acceptable for engineering design.

Table 4. Solution of Mathematical Model for Water Permeability Coefficient of Iron Phosphate Wastewater.

No.	Fitted Variable	Coefficient Name	Coefficient Value
1	T_e^2	a1	4.172×10^{-3}
2	C_f^2	a2	8.086×10^{-11}
3	F_p^2	a3	-1.344×10^{-2}
4	$T_e \times C_f$	a4	-1.576×10^{-6}
5	$C_f \times F_p$	a5	-1.54×10^{-7}
6	$T_e \times F_p$	a6	8.093×10^{-3}
7	T_e	a7	1.124×10^{-2}
8	C_f	a8	-2.038×10^{-5}
9	F_p	a9	1.779×10^{-1}
10	Constant	a10	6.3301

The model coefficients should be interpreted as empirical response-surface parameters rather than intrinsic membrane constants. The linear terms represent first-order effects of temperature, salinity, and flux; the quadratic terms describe nonlinear changes in permeability under concentrated wastewater conditions; and the interaction terms reflect coupled effects such as the simultaneous influence of salinity and flux on concentration polarization. Therefore, the model is applicable mainly within the experimental domain of T = 15–35 °C, C = 50–150 $g \cdot L^{-1}$, and F = 8–16 $L \cdot m^{-2} \cdot h^{-1}$, as well as to wastewater matrices similar to the iron phosphate wastewater studied here. Extrapolation beyond these ranges should be supported by additional pilot or field validation.

Sensitivity analysis indicates that the water permeability coefficient is most sensitive to temperature, with a sensitivity coefficient of 0.22, while the sensitivities to water flux and feed salt concentration are −0.14 and -4.2×10^{-6}, respectively. This response can be explained by the temperature dependence of solution viscosity, water mobility, and transient free-volume connectivity in the polyamide active layer, rather than by a permanent enlargement of membrane pores. Recent RO transport studies show that water permeation in polyamide membranes is strongly related to pressure-driven transport, polymer-matrix relaxation, and nanoscale water-diffusion pathways [30,31,34]. The model can provide guidance for optimizing RO operating parameters while controlling energy consumption.

Overall, the fitted model and engineering verification together support its use for preliminary pressure and flux design of high-salinity iron phosphate wastewater RO concentration systems within the validated operating range.

The predicted and experimental values and the relationships between A, temperature, feed salt concentration, and membrane surface flux are shown in Figures 7–9.

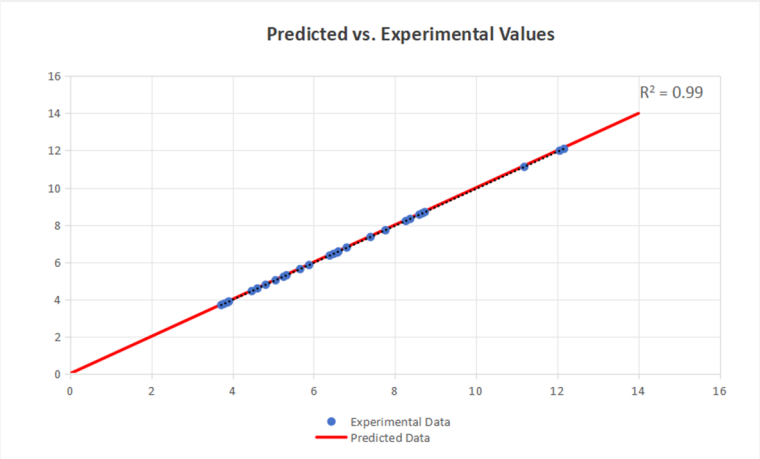

Figure 7. Predicted versus experimental values of the water permeability coefficient (A).

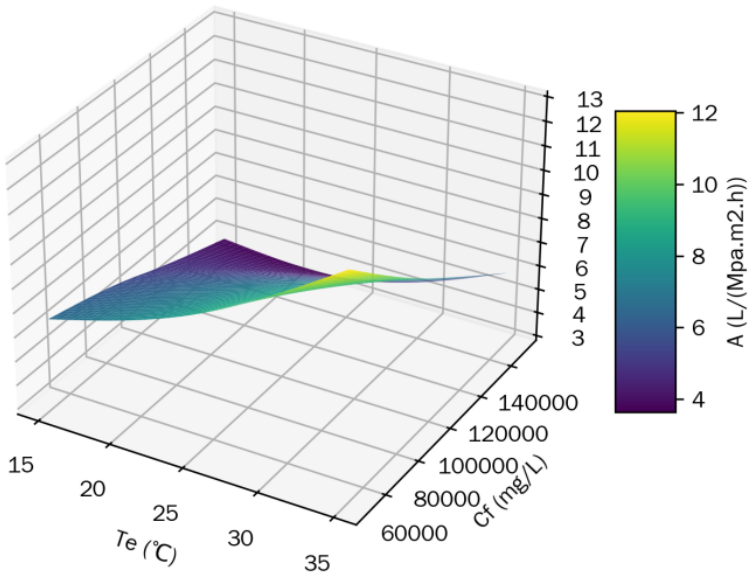

Figure 8. Relationship between water permeability coefficient A, temperature, and feed salt concentration.

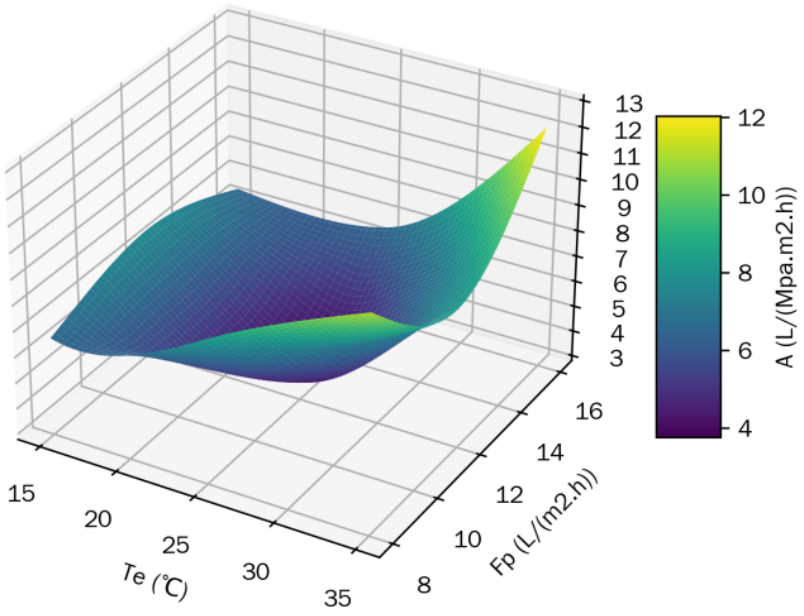

Figure 9. Relationship between water permeability coefficient A, temperature, and membrane surface flux.

3.3. Micro-osmosis Combined Membrane Process

To reduce reliance on energy-intensive evaporation, a micro-osmosis combined membrane process was proposed for high-efficiency concentration of iron phosphate wastewater.

Concentration experiments were carried out using the RO5+RO7 dual-membrane configuration, and the results are listed in Table 5. At an operating pressure of 8 MPa, the final concentrate concentration increased from 191.4 $g \cdot L^{-1}$ in the RO5+RO5 configuration to 206.1 $g \cdot L^{-1}$ in the RO5+RO7 configuration, corresponding to a concentration-endpoint improvement of 7.7% based on the measured values, or approximately 8.4% when rounded against the nominal 190 $g \cdot L^{-1}$ endpoint used in the process comparison. The improvement is attributed to the controlled salt passage of RO7, which raises permeate-side salinity and partially offsets the osmotic-pressure increase on the concentrate side. Therefore, the role of RO7 is not simply to act as another high-pressure RO stage, but to provide internal osmotic relief while maintaining an acceptable permeate quality for recycle or subsequent treatment.

Table 5. Concentrations of concentrate in micro-osmosis membrane combination process.

Feed Side Pressure	Final Concentrate Concentration		Permeate Side Average Salt Concentration	
	RO5+RO5	RO5+RO7	RO5+RO5	RO5+RO7
MPa	$g \cdot L^{-1}$	$g \cdot L^{-1}$	$mg \cdot L^{-1}$	$mg \cdot L^{-1}$
5.0	120	131	2520	5894
6.0	143	157	3067	6626
7.0	168	183	3629	7310
8.0	190	206	4188	7929

To clarify the calculation basis, the apparent water/salt balance at the 8 MPa endpoint was recalculated using Qf = Qc + Qp and QfCf = QcCc + QpCp, where Qf, Qc, and Qp are feed, concentrate, and permeate flow rates, respectively, and Cf, Cc, and Cp are the corresponding TDS concentrations. The feed TDS (150.0 $g \cdot L^{-1}$) and final concentrate TDS values (191.4 and 206.1 $g \cdot L^{-1}$) were interpreted according to the measured osmotic-pressure fitting curve described above. The RO5+RO7 permeate TDS of 7929 $mg \cdot L^{-1}$ (7.93 $g \cdot L^{-1}$) listed in Table 5 represents the average value of the mixed permeate, not the local permeate concentration at the terminal RO7 membrane. In the RO5+RO7 configuration, approximately 65% of the permeate was produced by the RO5 section with a TDS of about 4 $g \cdot L^{-1}$, whereas approximately 35% was produced by the RO7 section with a TDS of about 15 $g \cdot L^{-1}$; therefore, the mixed average was approximately 7.9 $g \cdot L^{-1}$. For estimating the NDP of the terminal membrane stage, the RO7-stage permeate TDS of about 15 $g \cdot L^{-1}$ was used because it better represents the permeate-side osmotic pressure acting across the final RO7 membrane.

The apparent mass-balance and terminal-membrane net-driving-pressure comparison at the 8 MPa endpoint is summarized in Table 6.

Table 6. Apparent mass-balance and terminal-membrane net-driving-pressure comparison at the 8 MPa endpoint.

Config.	Cf	Cc	Cp,mix	Cp,L	Y	ΔP	πc	πp,L	NDP,L
RO5+RO5	150.0	191.4	4.19	4.19	22.1	80	73.9	2.06	8.18
RO5+RO7	150.0	206.1	7.93	15.0	28.3	80	80.0	7.1	7.1
Hyp. RO*	150.0	206.1	4.19	4.19	27.8	80	80.0	2.06	2.06

Note: Cf, Cc, Cp,mix and Cp,L are expressed in g·L−1; ΔP, πc, πp,L and NDP,L are expressed in bar. Cp,mix is the measured average TDS of the mixed permeate, whereas Cp,L is the terminal-membrane permeate TDS used for NDP estimation. For RO5+RO7, Cp,mix = 7.93 $g \cdot L^{-1}$ represents the weighted average of RO5 permeate and RO7 permeate; Cp,L ≈ 15.0 $g \cdot L^{-1}$ represents the RO7-stage permeate TDS. Hyp. RO* is a hypothetical high-rejection RO element at 206.1 $g \cdot L^{-1}$ concentrate salinity with low terminal permeate salinity, used only to estimate the osmotic-relief contribution of RO7.

The recalculation shows that the higher TDS of the RO7 permeate increased the permeate-side osmotic pressure of the terminal membrane stage and thereby improved the terminal-stage NDP. When Cp,L ≈ 15.0 $g \cdot L^{-1}$ was used for the RO7 terminal stage, the estimated NDP remained at approximately 7.1 bar at the higher concentrate endpoint of 206.1 $g \cdot L^{-1}$, which was close to the 8.18 bar estimated for the RO5+RO5 configuration at 191.4 $g \cdot L^{-1}$. In contrast, if a high-rejection RO element with low permeate-side salinity were assumed at the same 206.1 $g \cdot L^{-1}$ concentrate salinity, the terminal-stage NDP would decrease to only approximately 2.06 bar. Therefore, RO7 did not simply increase the mixed permeate TDS; it increased the permeate-side osmotic pressure of the final membrane stage, maintained the terminal NDP above 6 bar, and enabled a higher concentration endpoint. This is the basis for reducing the downstream evaporation load and achieving the expected marginal energy-saving effect.

The reported energy-saving value should be understood as a marginal engineering estimate. It was calculated as $\Delta E = 0.084 \times 50 = 4.2\ kW \cdot h \cdot t^{-1}$, where 0.084 represents the fractional extension of the RO concentration endpoint and 50 $kW \cdot h \cdot t^{-1}$ represents the assumed energy-consumption difference between membrane concentration and evaporation for the marginal amount of water shifted from evaporation to RO treatment. Therefore, the value does not represent the total specific energy consumption of the whole system. A complete energy analysis should further include pump efficiency, pressure loss, actual recovery, circulation flow, and evaporator performance, which will be evaluated in future pilot-scale optimization.

3.4. Membrane Fouling Control

Long-term stable operation of membrane systems is restricted by membrane fouling; therefore, fouling characteristics and cleaning strategies were systematically analyzed. SEM comparison of virgin and fouled membranes showed substantial surface deposits on the fouled membrane (Figure 10), indicating complex mixed

fouling. SEM-EDS analysis detected Fe, Mn, Ca and other elements (Figure 11), suggesting that the foulants were mainly mixed inorganic scales such as calcium sulfate, manganese phosphate, and iron hydroxide. Such inorganic scaling can block effective transport pathways, reduce water permeability, and increase operating pressure, which is consistent with recent RO fouling studies [32].

For Fe-Mn-Ca composite fouling, a cleaning system combining chelation, dispersion, and acid–alkali synergy was designed. Tetrasodium EDTA acted as the main chelating agent and formed soluble complexes with Fe^{3+}, Mn^{2+}, and Ca^{2+}, thereby weakening the crystal structure of mixed scales. Ammonia water adjusted the cleaning solution to alkaline conditions and enhanced EDTA dissociation. Sodium hexametaphosphate served as a dispersant and supplementary chelating agent, preventing detached particles from re-aggregating or redepositing on the membrane surface. Secondary cleaning with 2% citric acid was used to remove residual metal hydroxide precipitates and restore the surface charge characteristics of the polyamide RO membrane. Compared with single-component cleaning systems, this multi-component sequence targeted the main inorganic foulants and improved both flux and salt-rejection recovery.

The changes in salt rejection and flux recovery after cleaning under different combinations are illustrated in Figure 12. Overall, secondary acid cleaning improved salt rejection, probably because it restored functional groups on the polyamide active layer that had been affected during alkaline cleaning. No obvious difference was observed between 2 h and 4 h soaking, indicating that the soaking time can be shortened to improve operational efficiency without sacrificing cleaning performance.

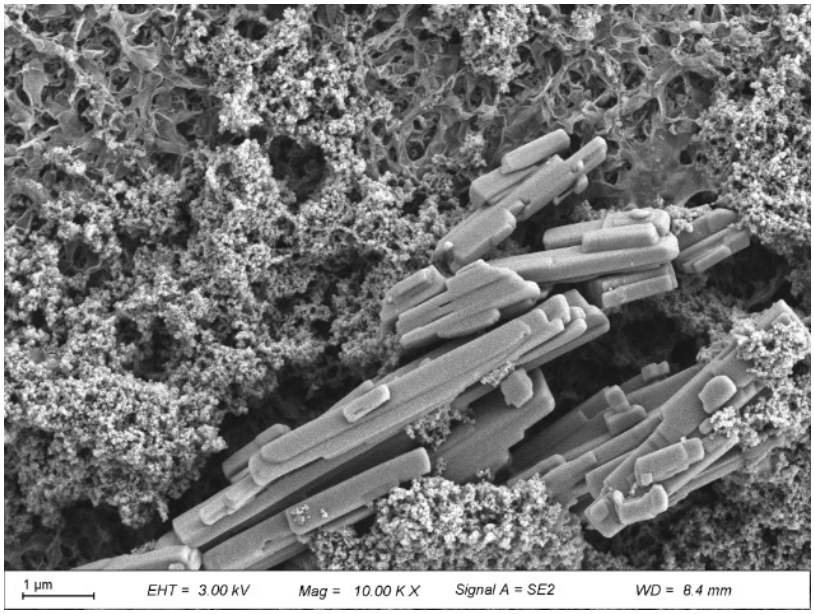

Figure 10. Morphology of Contaminants.

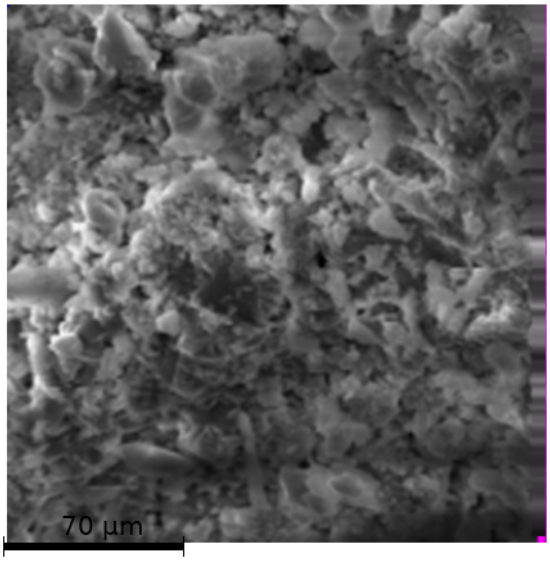

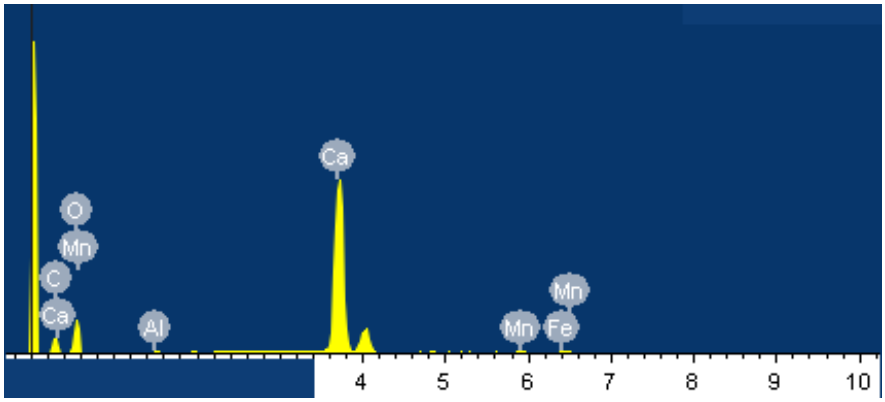

Figure 11. SEM image and EDS spectrum of contaminants.

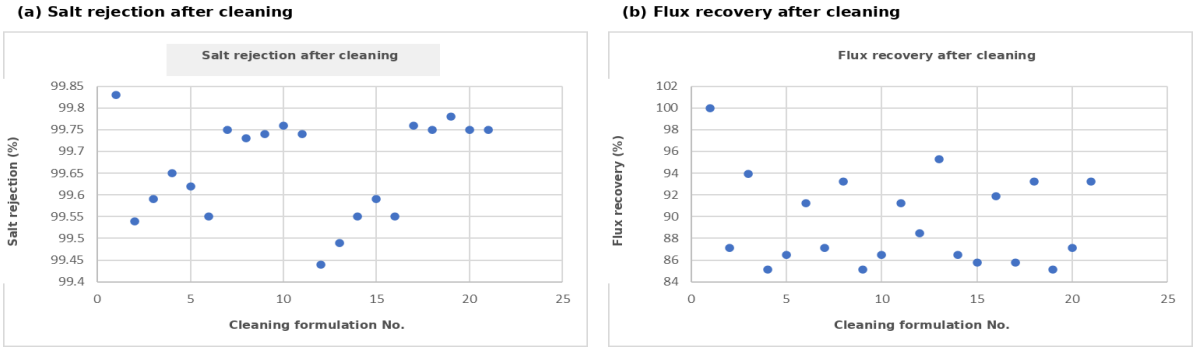

Figure 12. (**a**) Salt rejection after cleaning and (**b**) flux recovery after cleaning under different cleaning formulations.

Among all tested schemes, Formulations 17# and 20# exhibited the best performance. The optimal process consisted of alkaline cleaning with 1% tetrasodium EDTA + 0.5% ammonia water + 0.1% sodium hexametaphosphate, followed by secondary acid cleaning with 2% citric acid. The cleaning effect can be attributed to the combined action of EDTA chelation, alkaline solubilization, hexametaphosphate dispersion, and citric-acid removal of residual metal precipitates.

The high flux recovery should be interpreted in the context of the standardized post-cleaning membrane-performance test rather than as the operating flux at a feed salinity of approximately 200 $g \cdot L^{-1}$; in other words, the value of >94% represents cleaning recovery under the standard NaCl test and should not be interpreted as a high-salinity operating flux at the concentration endpoint. Before cleaning, the fouled membrane sheet showed a flux of 22.9 $L \cdot m^{-2} \cdot h^{-1}$ under the NaCl standard test, compared with 31 $L \cdot m^{-2} \cdot h^{-1}$ for a new membrane, corresponding to an initial recovery of approximately 74%. After targeted cleaning, the flux recovery increased to >94%, indicating that most of the resistance was caused by removable inorganic scaling instead of irreversible compaction or permanent damage of the polyamide active layer.

Additional operating records were analyzed to evaluate antifouling behavior, antifouling stability, and post-cleaning operational recovery. During operation at a feed pressure of 5.5 MPa, the average flux gradually decreased from 10.26 to 8.10 $L \cdot m^{-2} \cdot h^{-1}$ over the first operating period, while salt rejection remained stable at 99.50–99.70%. After cleaning, the flux recovered to approximately 9.9 $L \cdot m^{-2} \cdot h^{-1}$ and then gradually decreased during the following operating period, whereas salt rejection remained within 99.43–99.75%. These results indicate that the membrane retained stable salt-rejection performance and that the dominant fouling was largely reversible by the proposed chelation–dispersion/acid-cleaning sequence. The high recovery was also supported by pretreatment, which substantially reduced Fe, Mn, Ca/Mg, fluoride, and turbidity before RO concentration, thereby decreasing the load of irreversible particulate fouling.

4. Discussion

The flux recovery achieved in this study was higher than that reported for single-component cleaning agents [21], which can be attributed to the targeted chelation and dispersion of Fe-Mn-Ca composite scaling. The improvement in concentration endpoint is consistent with recent developments in advanced RO concentration and pressure-driven transport theory [16,30,31,34]. Compared with a conventional RO5+RO5 configuration, RO5+RO7 does not rely solely on increasing hydraulic pressure; instead, it uses controlled salt passage in the second stage to

reduce the osmotic-pressure penalty at high salinity. The engineering validation reported here refers to the permeability-coefficient model and was performed using DuPont SW30HRLE-400 seawater RO elements; the RO5+RO7 concentration-enhancement effect was evaluated separately using Veolia RO5 and RO7 elements under controlled staged-concentration tests. Nevertheless, the energy-saving calculation is only a marginal estimate and should be refined with full-scale pump-efficiency, recovery, pressure-loss, and evaporator-energy data.

Limitations and Future Prospects

This study systematically reveals the osmotic pressure characteristics, permeability coefficient variation law, process performance, and fouling control mechanism of iron phosphate wastewater in membrane separation systems.

Although favorable results were obtained under laboratory, staged-configuration, and engineering-verification conditions, several limitations remain. First, the experiments used real industrial wastewater, but the osmotic-pressure gradient was prepared from dried wastewater solids; possible loss of volatile components during drying should be considered when applying the osmotic-pressure model. Second, independent triplicate experiments were not performed because of the large sample volume and membrane-performance testing requirements; the reported values therefore represent stabilized operating data. Third, different RO membranes were used for different purposes: DuPont SW30XFR-400 membrane sheets and DuPont SW30HRLE-400 engineering elements were used for permeability-model fitting and validation, whereas Veolia RO5/RO7 elements were used to evaluate the staged concentration-enhancement effect through increased permeate-side salinity and reduced osmotic-pressure difference. Fourth, the fouling-control study demonstrated short-term cleaning performance and operating stability, but repeated cleaning cycles, long-term membrane aging, and irreversible fouling accumulation still require further investigation. Finally, the permeability and osmotic-pressure models were established within specific temperature, concentration, and flux ranges, and extrapolation beyond these ranges should be supported by additional pilot or field data.

Future research directions include:

(1) Developing more efficient and eco-friendly membrane materials and cleaning agents to reduce membrane fouling and operational costs;
(2) Integrating artificial intelligence for real-time monitoring and intelligent control of the membrane separation process to improve automation;
(3) Conducting life cycle assessment to comprehensively evaluate the environmental and economic benefits of the micro-osmosis combined process.

5. Conclusions

This study demonstrates the feasibility of RO concentration for real high-salinity iron phosphate wastewater by integrating osmotic-pressure measurement, permeability prediction, RO5+RO7 configuration optimization, and fouling-specific cleaning. The main conclusions are as follows:

(1) High-salinity iron phosphate wastewater shows non-ideal osmotic-pressure behavior; incorporating activity-coefficient effects improves pressure estimation for RO design.
(2) The ternary quadratic permeability model captures the combined effects of temperature, membrane surface flux, and feed salinity within the tested range. Engineering-scale verification gave a predicted permeate flow close to the actual value and a pressure deviation below 5%, supporting its use for preliminary process design.
(3) The RO5+RO7 configuration differs from conventional staged RO by using a lower-rejection second-stage RO element to provide internal osmotic relief without an external draw solution. This configuration increased the practical concentration endpoint to approximately 206 $g \cdot L^{-1}$ under the 8 MPa pressure limit.
(4) SEM-EDS confirmed Fe-Mn-Ca composite scaling as the main fouling type. The chelation–dispersion/acid-cleaning sequence restored flux recovery to >94% under standard test conditions while maintaining high salt rejection, indicating that the dominant fouling was largely reversible. Further work should verify repeated cleaning cycles, long-term membrane aging, and complete energy consumption at pilot or full scale.

Author Contributions

X.Y.: conceptualization, supervision, project administration, and writing—review and editing; S.K.: writing—review and editing, visualization, and data processing; M.D.: validation and formal analysis; H.C.: visualization and data checking; Y.W.: methodology, investigation, data curation, visualization, and writing—original draft preparation. All authors have read and agreed to the published version of the manuscript.

Funding

The APC was funded by the National Natural Science Foundation of China (No. 42467011), the Humanities and Social Sciences Project of Jiangxi Provincial Department of Education (No. JC22135), and the Open Fund of Jiangxi Key Laboratory of Atmospheric Pollution Causes and Control (No. AE2102).

Institutional Review Board Statement

Not applicable.

Informed Consent Statement

Not applicable.

Data Availability Statement

The data presented in this study are available from the corresponding author upon reasonable request.

Conflicts of Interest

The authors declare no conflict of interest.

Use of AI and AI-Assisted Technologies

During the preparation of this work, the authors used AI to assist with language polishing, formatting checks, and proofreading. After using this tool, the authors reviewed and edited the content as needed and take full responsibility for the content of the published article.

References

1. Prosini, P.P.; Carewska, M.; Scaccia, S.; et al. Long-Term Cyclability of Nanostructured $LiFePO_4$. *Electrochim. Acta* **2003**, *48*, 4205–4211.
2. Zhang, T.; Lin, S.; Yu, J.G. Research Progress in Preparation and Performance Enhancement of Lithium Iron Phosphate Cathode Materials. *Inorg. Chem. Ind.* **2021**, *53*, 31–40. https://doi.org/10.19964/j.issn.1006-4990.2021-0212. (In Chinese)
3. Yao, J.; Bewlay, S.; Konstantinov, K.; et al. Characterisation of Olivine-Type $LiMn_xFe_{1-x}PO_4$ Cathode Materials. *J. Alloys Compd.* **2006**, *425*, 362–366.
4. Zhang, B.Q.; Wang, S.Z.; Liu, L.; et al. Growth Mechanism of Nano-Lithium Iron Phosphate Crystals Synthesized by Supercritical Solvothermal Method. *J. Xi'an Jiaotong Univ.* **2023**, *57*, 100–109. https://doi.org/10.7652/xjtuxb202302011. (In Chinese)
5. Ma, G.X.; Liu, R.; Liu, H.Q.; et al. Study on Lithium Manganese Iron Phosphate Cathode Materials Coated with Different Carbon Contents. *J. Shandong Univ. Sci. Technol. Nat. Sci.* **2020**, *39*, 42–48. https://doi.org/10.16452/j.cnki.sdkjzk.2020.06.005. (In Chinese)
6. Qiu, P.; Yang, M.L.; Wang, B.W. Research Progress in Synthesis of Nano-Lithium Iron Phosphate. *Chin. J. Power Sources* **2012**, *36*, 1576–1578. (In Chinese)
7. Di, Y.X.; Yu, L. Study on Properties of Nanometer Lithium Iron Phosphate Synthesized by Explosive Detonation. *Eng. Blasting* **2014**, *20*, 36–38,57. https://doi.org/10.3969/j.issn.1006-7051.2014.06.009. (In Chinese)
8. Wang, Z.H.; Li, J.; Chen, M.; et al. Process Study on Battery-Grade Iron Phosphate Prepared by Co-Precipitation of Ferric Nitrate and Phosphoric Acid. *Inorg. Salt Ind.* **2023**, *55*, 51–57. https://doi.org/10.19964/j.issn.1006-4990.2022-0548. (In Chinese)
9. Wu, C.Z.; Wu, C.W.; Zhang, M.X. Discussion on Zero-Discharge Treatment Process of Production Wastewater in the Iron Phosphate Industry. *Water Pollut. Treat.* **2024**, *12*, 23–27. https://doi.org/10.12677/wpt.2024.123004. (In Chinese)
10. Chang, Y.; Wang, X.; Zhao, B.; et al. Green and High-Yield Recovery of Phosphorus from Municipal Wastewater for $LiFePO_4$ Batteries. *Engineering* **2025**, *45*, 234–242. https://doi.org/10.1016/j.eng.2024.05.018.
11. Chen, T.; Li, M.; Bae, J. Recent Advances in Lithium Iron Phosphate Battery Technology: A Comprehensive Review. *Batteries* **2024**, *10*, 424.
12. Müller, M.; Obuz, H.E.; Keber, S.; et al. Concepts for the Sustainable Hydrometallurgical Processing of End-of-Life Lithium Iron Phosphate (LFP) Batteries. *Sustainability* **2024**, *16*, 11267.
13. Elimelech, M.; Phillip, W.A. The Future of Seawater Desalination: Energy, Technology, and the Environment. *Science* **2011**, *333*, 712–717.

14. Yu, X.J.; Wu, S.W.; Zhu, Y.Y.; et al. Application and Research Progress of Humidification-Dehumidification Technology in High-Salinity Wastewater Concentration. *Water Treat. Technol.* **2021**, *47*, 18–23,33. https://doi.org/10.16796/j.cnki.1000-3770.2021.06.004. (In Chinese)
15. Liu, M.J.; Gong, F.Z.; Tie, Y.F.; et al. Study on Zero-Discharge Process of Wastewater from Iron Phosphate Production Treated by Reverse Osmosis Membrane Method. *Inorg. Salt Ind.* **2021**, *53*, 101–105. https://doi.org/10.19964/j.issn.1006-4990.2020-0531. (In Chinese)
16. Warsinger, D.M.; Tow, E.W.; Nayar, K.G.; et al. Energy Efficiency of Batch and Semi-Batch (CCRO) Reverse Osmosis Desalination. *Water Res.* **2016**, *106*, 272–282.
17. Zhang, T.; Zhang, Z.C. Causes and Countermeasures of Decreased Salt Rejection in Reverse Osmosis Membrane Treatment of Ammonium-Process Iron Phosphate Industrial Wastewater. *Yunnan Chem. Technol.* **2025**, *52*, 112–116. https://doi.org/10.3969/j.issn.1004-275X.2025.11.25. (In Chinese)
18. Ding, H.L.; Zhao, P.S.; Wang, X.L. Application of Concentration and Reduction Process in Zero Discharge of Industrial Wastewater. *Mod. Chem. Res.* **2025**, *22*, 182–184. https://doi.org/10.20087/j.cnki.1672-8114.2025.22.059. (In Chinese)
19. Ma, J.; Lin, Z.F.; Chen, M.L.; et al. Application Research of Nanofiltration-Reverse Osmosis Combined Membrane Process in Treatment and Reuse of Electroplating Wastewater. *Environ. Prot.* **2008**, *18*, 72–73. https://doi.org/10.14026/j.cnki.0253-9705.2008.18.012. (In Chinese)
20. Song, Y.G.; Zhang, Y.F.; Deng, M.M.; et al. Study on Membrane Fouling Control of High-Efficiency Reverse Osmosis Process for High-Salinity Coal Chemical Wastewater Treatment. *Process Ind.* **2025**, *9*, 68–70. (In Chinese)
21. Li, H.; Song, B.; Song, J.Z.; et al. Compounding of Cleaning Agent for Reverse Osmosis Membrane and Its Application. *Environ. Prot. Chem. Ind.* **2026**, *46*, 234–241. https://doi.org/10.3969/j.issn.1006-1878.2026.02.012. (In Chinese)
22. Jin, R.X.; Liu, X.; Zhang, Z.L.; et al. Research Progress of Membrane Treatment Technology for High-Salinity Wastewater. *Ind. Water Treat.* **2026**. https://doi.org/10.19965/j.cnki.iwt.2025-0600. (In Chinese)
23. Meng, X.H.; Zhu, H.W. Prediction of Permeability Coefficient of Ordinary Pervious Concrete Based on Machine Learning. *Highway Eng.* **2025**, *50*, 184–191. https://doi.org/10.19782/j.cnki.1674-0610.2025. (In Chinese)
24. Qian, T.; Lu, D.; Zhang, Y.Q.; et al. Progress in Particle Fouling Mechanism and CFD Simulation of Pressure-Driven Membrane Processes. *Membr. Sci. Technol.* **2024**, *44*, 158–168. https://doi.org/10.16159/j.cnki.issn1007-8924.2024.06.018. (In Chinese)
25. Ma, W.J. Study on the Influence of Backwash Water Ion Components on Ultrafiltration Membrane Fouling and Effluent Biological Safety Stability. Master's Thesis, Harbin Institute of Technology, Harbin, China, 2025. https://doi.org/10.27061/d.cnki.ghgdu.2025.003194. (In Chinese)
26. Li, T.; Lin, X.; Na, J.; et al. Accelerating Hydrogen Evolution Rate and Preventing Metal Hydroxide Deposition in Seawater Electrolysis via Addition of Chelating Agent EDTA-Na_4. *J. Energy Chem.* **2026**, *114*, 686–698.
27. Wang, J.Y. Analysis of Fouling Characteristics of Retired Desalination Membranes and Research on Efficient Membrane Cleaning Strategies. Master's Thesis, Zhejiang University, Zhejiang, China, 2023. https://doi.org/10.27461/d.cnki.gzjdx.2023. (In Chinese)
28. Li, P.R.; Hu, C.S.; Wang, J.Q.; et al. Research Progress on Treatment Technology of Lithium Iron Phosphate Wastewater. *Jiangxi Chem. Ind.* **2025**, 41, 81–84. (In Chinese)
29. Pan, C.L.; Shu, Z.H.; Cai, B.X.; et al. Exploration on Key Membrane Treatment Technologies and Resource Utilization of High-Salinity Wastewater. *Leather Manuf. Environ. Prot. Technol.* **2023**, *4*, 18–19,22. https://doi.org/10.20025/j.cnki.CN10-1679.2023-12-05. (In Chinese)
30. Heiranian, M.; Fan, H.; Wang, L.; et al. Mechanisms and Models for Water Transport in Reverse Osmosis Membranes: History, Critical Assessment, and Recent Developments. *Chem. Soc. Rev.* **2023**, *52*, 8455–8480. https://doi.org/10.1039/D3CS00395G.
31. Wang, L.; He, J.; Heiranian, M.; et al. Water Transport in Reverse Osmosis Membranes Is Governed by Pore Flow, Not a Solution-Diffusion Mechanism. *Sci. Adv.* **2023**, *9*, eadf8488. https://doi.org/10.1126/sciadv.adf8488.
32. Ahmed, M.A.; Amin, S.; Mohamed, A.A. Fouling in Reverse Osmosis Membranes: Monitoring, Characterization, Mitigation Strategies and Future Directions. *Heliyon* **2023**, *9*, e14908. https://doi.org/10.1016/j.heliyon.2023.e14908.
33. Clegg, S.L.; Waters, J.F.; Turner, D.R.; et al. Chemical Speciation Models Based upon the Pitzer Activity Coefficient Equations, Including the Propagation of Uncertainties. III. Seawater from the Freezing Point to 45 °C, Including Acid-Base Equilibria. *Mar. Chem.* **2023**, *250*, 104196. https://doi.org/10.1016/j.marchem.2022.104196.
34. Foglia, F.; Frick, B.; Nania, M.; et al. Multimodal Confined Water Dynamics in Reverse Osmosis Polyamide Membranes. *Nat. Commun.* **2022**, *13*, 2809. https://doi.org/10.1038/s41467-022-30555-6.
35. DuPont Water Solutions. FilmTec™ SW30XFR-400/34i Element. Available online: https://www.dupont.com/content/dam/water/amer/us/en/water/public/documents/en/RO-FilmTec-SW30XFR-400-34i-PDS-45-D00700-en.pdf (accessed on 12 March 2026).
36. Veolia Water Technologies. *Industrial RO Series*; Veolia Water Technologies: Trevose, PA, USA, 2023. Available online: https://preprod.watertechnologies.com/document/document/contentdownload/?document_name=FSsmIndustrialROSeries_EN.pdf&language=English&security=Public (accessed on 12 March 2026).